EES Batteries

PAPER

View Article Online
View Journal

Cite this: DOI: 10.1039/d6eb00011h

Towards safer electrolytes: comparing the air stability and electrochemical properties of $NaPF_6$, NaTFSI and $Na[B(hfip)_4]$·DME for sodium-ion batteries

Darren M. C. Ould,[a,f] James M. Courtney,[a] David J. Morgan,[b,c] Daniel J. Curtis,[a] Marcin W. Orzech,[a] Sajad Kiani,[a] Brent de Boode,[d] Clare P. Grey,[e,f] Dominic S. Wright[e,f] and Serena Margadonna *[a]

Sodium-ion batteries (SIBs) are a promising post lithium-ion battery (LIB) technology, which offer advantages in improved sustainability. This work investigates using NaTFSI [TFSI = bis(trifluoromethylsulfonyl) imide] and $Na[B(hfip)_4]$·DME [hfip = $OCH(CF_3)_2$ (O^iPr^F), DME = 1,2-dimethoxyethane] as alternative electrolyte salts to the current benchmark standard $NaPF_6$ and compares their air stability, electrochemical properties and performance in sodium-ion coin cells. Multinuclear NMR spectroscopic experiments found that $NaPF_6$ and NaTFSI were stable to atmospheric air after one month, whereas $Na[B(hfip)_4]$·DME showed signs of degradation. The air stability of $NaPF_6$ was compared to $LiPF_6$, where the latter underwent complete decomposition after 24 hours. Electrochemical investigations in 1 M solutions of ethylene carbonate : diethyl carbonate (EC : DEC) solvent revealed 1 M $NaPF_6$ has the highest bulk conductivity. Cyclic voltammetry experiments showed 1 M $NaPF_6$ and 1 M $Na[B(hfip)_4]$·DME are compatible with aluminium foils up to 4.2 V *vs.* Na/Na^+, whereas 1 M NaTFSI underwent aluminium corrosion. Corrosion could be supressed by either limiting cut-off voltage or by the addition of 2 wt% $NaPF_6$ as an additive, both applicable mitigation strategies. Stable long-term cycling at 1C rate in cells using a Prussian white cathode and hard carbon anode occured with both 1 M $NaPF_6$ and 1 M NaTFSI electrolytes. Thus, 1 M NaTFSI is a viable alternative to 1 M $NaPF_6$ in SIBs with a Prussian white cathode, offering a potentially safer electrolyte choice by limiting HF generation on account of the strong C–F bonds in NaTFSI.

Received 16th January 2026,
Accepted 21st January 2026

DOI: 10.1039/d6eb00011h

rsc.li/EESBatteries

Broader context

Due to the growing demand for energy storage devices, more sustainable alternatives to lithium-ion batteries are required. Sodium-ion batteries are a promising emerging battery technology that have improved sustainability, given the wider abundance of sodium. For the electrolyte, $NaPF_6$ (appropriated from lithium-ion batteries which commonly use $LiPF_6$) is frequently used as the salt. However, during battery cycling $NaPF_6$ degrades to release toxic HF, which causes severe safety concerns and adds challenges to battery recycling.

This work has investigated using NaTFSI and $Na[B(hfip)_4]$·DME [hfip = $OCH(CF_3)_2$, DME = 1,2-dimethoxyethane] as alternative electrolyte salts which are less prone to HF formation, on account of strong C–F bonds. The fundamental properties of these salts have been compared and importantly it was found that $NaPF_6$ possesses remarkable air stability. Using NMR spectroscopy, no signs of decomposition occurred after one month of air exposure, whereas in contrast $LiPF_6$ fully decomposed after 24 hours. The high air tolerance of $NaPF_6$ means expensive transport of the salt under inert atmosphere may not be necessary. Long-term cycling in full-cells containing a Prussian white cathode showed 1 M NaTFSI in carbonate solvent cycles comparably to 1 M $NaPF_6$, paving the way for high-performing, safer and lower-cost sodium-ion batteries.

[a]*Department of Chemical Engineering, Faculty of Science and Engineering, Swansea University, Swansea SA1 8EN, UK. E-mail: S.Margadonna@Swansea.ac.uk*
[b]*Department of Chemistry, Translational Research Hub, Cardiff University, Maindy Road, Cardiff CF24 3AT, UK*
[c]*HarwellXPS, Research Complex at Harwell, Didcot, Oxon OX11 3FA, UK*
[d]*Batri Ltd., Unit 6a Bridgend Business Centre, Bennett Street, Bridgend, CF31 3SH, UK*
[e]*Yusuf Hamied Department of Chemistry, University of Cambridge, Lensfield Road, Cambridge, CB2 1EW, UK*
[f]*The Faraday Institution, Quad One, Harwell Science and Innovation Campus, Didcot, OX11 ORA, UK*

Introduction

As the world transitions to net zero economies, suitable energy storage technologies are required. Currently, lithium-ion batteries (LIBs) lead the way in rechargeable battery technology.[1,2] However, they depend on resource-critical materials, such as lithium, nickel and cobalt, which causes concerns regarding their long-term sustainability.[3,4] Sodium-ion batteries (SIBs) are a promising emerging rechargeable battery technology that are more sustainable and are suited for home energy storage and large scale load-levelling. Unlike lithium, sodium deposits are widely abundant and evenly distributed across the globe. Moreover, SIBs allow cobalt-free cathodes to be used, for example Prussian white ($Na_2Fe[Fe(CN)_6]$),[3,4] and hard carbon is commonly used for the anode.[5,6]

A key advantage for SIBs is the cathode material can be constructed from inexpensive and noncritical transition metals. While layered transition metal oxide cathodes remain popular, they face challenges including irreversible phase transitions during battery operation and poor air stability. Prussian blue analogues (PBAs) are an alternative cathode material of general formula $A_xM_1[M_2(CN)_6]\cdot nH_2O$ (A = alkali–metal ion, M_1 and M_2 = transition metals).[7] Prussian white, $Na_2Fe[Fe(CN)_6]$, cathodes are attractive for SIBs due to their large ion diffusion channels, low cost, high theoretical capacity and non-toxicity.[8]

The electrolyte solution plays a crucial role in a battery, as it is largely responsible for the accessible capacity, overall lifetime, safety implications and manufacturing limitations.[9] SIB electrolytes have largely followed the direction of LIB electrolytes and 1 M sodium hexafluorophosphate ($NaPF_6$) in carbonate solvent has become the benchmark electrolyte. This is due to $NaPF_6$ offering the best compromise of ionic conductivity, thermal stability, chemical stability, safety and cost.[10] Moreover, the preferential decomposition of the PF_6^- anion during battery cycling, which generates a thin, inorganic-rich electrode–electrolyte interphase, ensures both interphase and electrode stability and prevents further solvent decomposition.[11] Nevertheless, a significant drawback of using $NaPF_6$ is its ability to form toxic decomposition products, such as HF, POF_3 and $PO_2F_2^-$.[12] The presence of HF has been detected by NMR spectroscopy in battery-grade electrolytes containing <20 ppm water.[12] The generation of toxic breakdown products using $NaPF_6$ creates safety concerns and adds additional challenges to battery recycling.

Sodium perchlorate ($NaClO_4$) is an alternative and commonly used electrolyte salt for SIBs, which is popular due to its fast ion migration and low cost. Despite this, the use of $NaClO_4$ poses safety concerns due to the oxidising properties of the ClO_4^- anion, which limits its industrial application. Additionally, it has been shown that using $NaPF_6$-based carbonate electrolyte outperforms $NaClO_4$-based carbonate electrolyte at high-rate battery cycling.[11] Using Raman spectroscopy, it was found that the Na^+–solvent interaction of the electrolytes in propylene carbonate : ethyl methyl carbonate : dimethyl carbonate : fluoroethylene carbonate (PC : EMC : DMC : FEC, 30 : 30 : 40 : 2 v/v) solvent was stronger for $NaClO_4$ than $NaPF_6$, leading to a higher desolvation energy and a slower desolvation process. Moreover, while both the PF_6^- anion and ClO_4^- anion participated in the solvation structure of Na^+, the binding between Na^+ and PF_6^- was weaker than in Na^+ and ClO_4^-. Lastly, the preferential decomposition of the PF_6^- anion to form a thin, inorganic-rich cathode-electrolyte interphase (CEI), compared to the thicker and uneven CEI generated when using $NaClO_4$, helped explain the better cycling performance using $NaPF_6$ as the electrolyte salt.[11]

Sodium salts containing sulfonyl imide functionality, including sodium bis(fluorosulfonyl)imide (NaFSI) and sodium bis(trifluoromethylsulfonyl)imide (NaTFSI), are promising electrolyte salts as they are non-toxic and have high thermal stabilities. However, they are seldom used alone as the electrolyte salt due to incompatibility with aluminium current collectors commonly used for both the anode and cathode in SIBs. Corrosion of aluminium current collectors when using the FSI^- anion has been extensively studied,[13–16] but fewer studies have investigated the corrosion processes when using NaTFSI. NaFSI and NaTFSI remain popular salt choices when combined with room-temperature ionic liquid solvents, due to affording good ionic conductivity and a wide electrochemical stability window (ESW).[17,18]

Previously, NaFSI has been reported to have good tolerance to aqueous conditions (greater than LiFSI) and in the same work, the $TFSI^-$ anion was hypothesised to have even greater chemical stability.[19] This is on account of the stronger C–F bond strength in $TFSI^-$ compared to the weaker S–F bond strength in the FSI^- anion. Furthermore, computational studies have revealed HF release by hydrolysis in LiTFSI is very limited compared to $LiPF_6$ and LiFSI.[20]

The fundamental properties of $NaPF_6$ and NaTFSI electrolytes in ethylene carbonate : dimethyl carbonate (EC : DMC) have previously been compared at different concentrations,[21] where it was found that both electrolytes had liquid ranges between −30 °C to at least 40 °C. In EC : DMC solvent, $NaPF_6$ reached a maximum ionic conductivity value of 11.2 mS cm^{-1} at 1.2 M concentration, whereas NaTFSI reached a reached a maximum ionic conductivity value of 8.5 mS cm^{-1} at a lower concentration, 1.0 M. In the same study, using Raman spectroscopy it was determined that NaTFSI-based electrolytes have more contact ion-pairs than when using $NaPF_6$ as the electrolyte salt and is less dissociated.[21] These findings were in agreement with an earlier study which also compared $NaPF_6$ and NaTFSI electrolyte salts in different solvents.[10] The ionic conductivity was similar but higher when using 1 M $NaPF_6$ in propylene carbonate (PC) solvent than 1 M NaTFSI in PC, 7.98 mS cm^{-1} and 6.2 mS cm^{-1}, respectively. In addition, 1 M $NaPF_6$ in PC solvent was found to be more thermally stable than 1 M NaTFSI in PC, 280 °C and 250 °C, respectively. 1 M NaTFSI in PC promoted corrosion of the aluminium foil when used as the working electrode in cyclic voltammetry (CV) experiments.[10]

Recently, new electrolyte salts have been reported for use in SIBs. Sodium bis(oxalato)borate, Na[BOB] [BOB = bis(oxalato)

borate], has been shown to be a promising non-fluorinated electrolyte salt when used with trimethyl phosphate (TMP), *N*-methyl-2-pyrrolidone (NMP), or mixtures of these solvents in cells containing a Prussian white cathode and hard carbon anode.[22–24] Additionally, NaBOB is an effective electrolyte additive.[25] However, the solubility of the BOB^- anion is low in traditionally used carbonate battery solvents. To improve the solubility, the related sodium-difluoro(oxalato)borate (NaDFOB) salt can be used and 1 M NaDFOB in diglyme solvent has recently been reported to give stable long-term cycling, even across a temperature window of −20 °C to 60 °C, in cells using a $Na_4Fe_3(PO_4)_2P_2O_7$ (NFPP) cathode and hard carbon anode.[26] In addition, a low-concentration electrolyte containing NaDFOB in TMP solvent has been reported to enable long-term cycling in cells using a $Na_3V_2(PO_4)_3$ cathode and sodium metal anode.[27] NaDFOB may also be used as an electrolyte additive, where it has been shown to restrain the growth of sodium dendrites in cells containing an FeMn-based Prussian blue cathode and hard carbon anode.[28]

Alternatively, a series of sodium borate electrolyte salts containing $[B(OR)_n]^-$ (R = fluorinated ligand, n = 2 or 4) anions has been reported. Na[B(hfip)$_4$]·DME [hfip = $OCH(CF_3)_2$ (O^iPr^F), DME = 1,2-dimethoxyethane] was found to offer stable cycling in cells using a $[Ni_{(0.27\pm0.05)}Mn_{(0.42\pm0.05)}Mg_{(0.15\pm0.05)}Ti_{(0.17\pm0.05)}]O_{(2\pm0.05)}$ cathode and hard carbon anode, as well as providing a stable solid-electrolyte interphase (SEI).[29] Interestingly, the lithium analogue of this salt, Li[B(hfip)$_4$]·3DME, has been demonstrated to be a promising candidate in next-generation high voltage lithium batteries, where 1 M Li[B(hfip)$_4$]·3DME in EC : DMC (1 : 1 v/v) electrolyte gave high oxidative stability when using aluminium and glassy carbon electrodes. This was explained due to a highly stable passivation layer on aluminium forming when using this electrolyte.[30] In addition, the $[B(hfip)_4]^-$ anion has been used in both magnesium-ion and calcium-ion batteries.[31–34]

This work investigates the use of NaTFSI and sodium tetrakis(hexafluoroisopropoxy)borate, Na[B(hfip)$_4$]·DME, as alternative electrolyte salts to the benchmark $NaPF_6$ for use in SIBs (Fig. 1). The air stability, electrochemical properties and sodium-ion cycling performance of all three sodium electrolyte salts have been studied and compared. It was found that both $NaPF_6$ and NaTFSI salts are stable to atmospheric air, whereas Na[B(hfip)$_4$]·DME underwent decomposition. The air stability of $NaPF_6$ was compared to $LiPF_6$, where the latter decomposed after 24 hours, highlighting stark differences in the air stabilities of PF_6-based salts. Electrochemical experiments showed 1 M $NaPF_6$ in ethylene carbonate : diethyl carbonate (EC : DEC 1 : 1 v/v) has the highest bulk conductivity, whereas cyclic voltammetry (CV) experiments using 1 M NaTFSI in EC : DEC causes corrosion on aluminium foils. Corrosion could be suppressed by either cycling at lower voltages or by adding 2 wt% $NaPF_6$ as an additive. Nevertheless, 1 M NaTFSI cycled comparably to 1 M $NaPF_6$ in sodium-ion coin cells using a Prussian white cathode and hard carbon anode. Use of 1 M NaTFSI with cells containing an inexpensive Prussian white cathode offers a potential route to a safer electrolyte solution which is less prone to HF release, on account of the strong C–F bonds in NaTFSI.

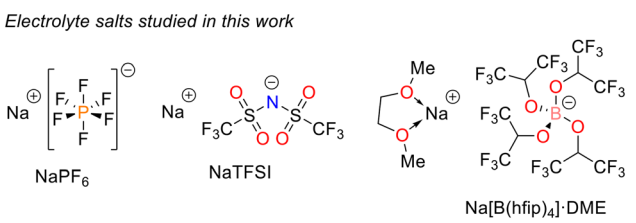

Fig. 1 Structures of the electrolyte salts studied in this work, $NaPF_6$, NaTFSI and Na[B(hfip)$_4$]·DME [hfip = $OCH(CF_3)_2$ (O^iPr^F), DME = 1,2-dimethoxyethane].

Results and discussion

An electrolyte salt that has a high tolerance to air is beneficial as this affords safe and convenient handling, transport and storage, in turn reducing manufacturing costs. We first investigated the stability of the electrolyte salts $NaPF_6$, NaTFSI and Na[B(hfip)$_4$]·DME towards atmospheric air. 0.1 mmol of the salts were exposed to ambient air in uncapped plastic vials at room temperature (17–20 °C, 30–55% relative humidity) in the fume hood of the laboratory for 1 day, 1 week (7 days) and 1 month (30 days). The air exposed salts were then dissolved in DMSO-d_6 solvent and multinuclear solution-state NMR spectroscopic studies were performed (Fig. 2).

^{19}F, ^{31}P and ^{11}B NMR spectroscopy revealed that no significant decomposition of $NaPF_6$, NaTFSI and Na[B(hfip)$_4$]·DME had taken place after 1 day. However, while no degradation of $NaPF_6$ and NaTFSI (likely on account of strong C–F bonds present in NaTFSI) was observed after 1 month of air exposure (Fig. 2a and b), after 7 days a small amount of insoluble solid decomposition product was observed for Na[B(hfip)$_4$]·DME, the amount of which increased over 1 month of air exposure. After 1 month, ^{19}F NMR spectroscopy showed the presence of degradation products of the $[B(hfip)_4]^-$ anion (Fig. 2c), with the appearance of low-intensity signals at −69.4 ppm and −70.9 ppm, indicative of a $-CF_3$ group. No changes were observed in the ^{11}B NMR spectra for Na[B(hfip)$_4$]·DME (Fig. S71), but a very low intensity signal at 1.6 ppm was observed after one month of air exposure, supporting the finding of salt decomposition. The ^{31}P NMR spectra for the $NaPF_6$ air exposed samples are shown in Fig. S64 and show retention of the septet at −144.2 ppm throughout the 1 month air exposure experiment, corresponding to the PF_6^- anion.

Given the popularity of using $LiPF_6$ as the electrolyte salt for LIBs, the air stabilities of $LiPF_6$ and $NaPF_6$ were compared. In contrast to $NaPF_6$, after leaving pristine $LiPF_6$ exposed to air in a plastic vial for 1 day, complete decomposition of the PF_6^- anion had occurred. The ^{19}F NMR spectrum (Fig. 3a) revealed a low intensity (low signal to noise) doublet at −70.1 ppm ($^1J_{PF}$ = 711 Hz), assigned to residual $LiPF_6$. Accordingly, the ^{31}P

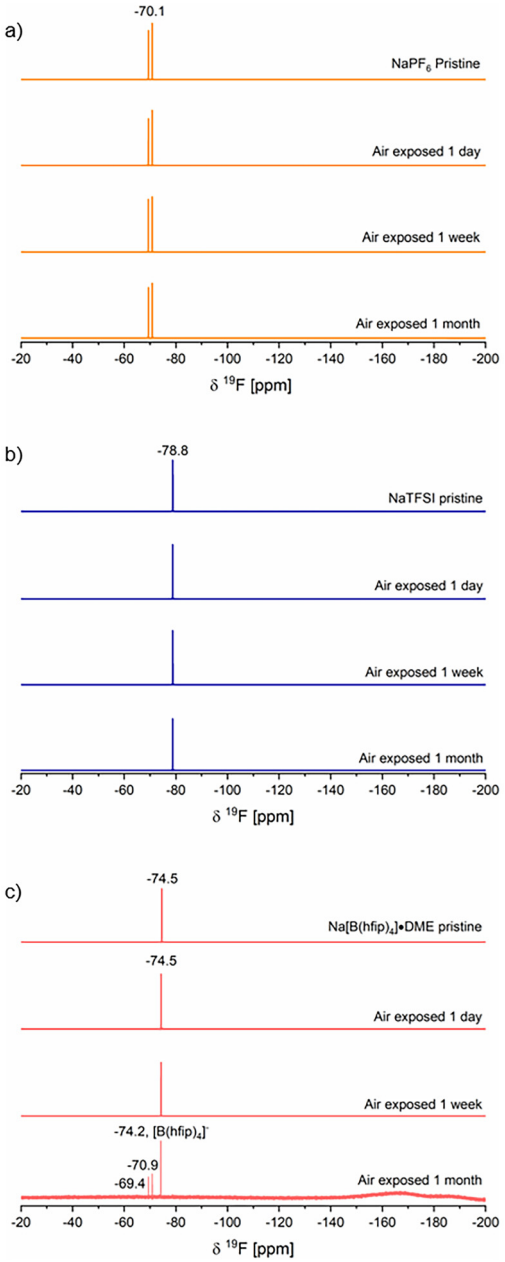

Fig. 2 ^{19}F NMR (471 MHz, $(CD_3)_2SO$, 295 K) of the soluble products after leaving 0.1 mmol of the salts $NaPF_6$ (a, orange), NaTFSI (b, blue) and $Na[B(hfip)_4]$·DME (c, pink) exposed to atmospheric air in an uncapped vial at room temperature (17–20 °C) for 1 day (24 hours), 1 week (7 days) and 1 month (30 days).

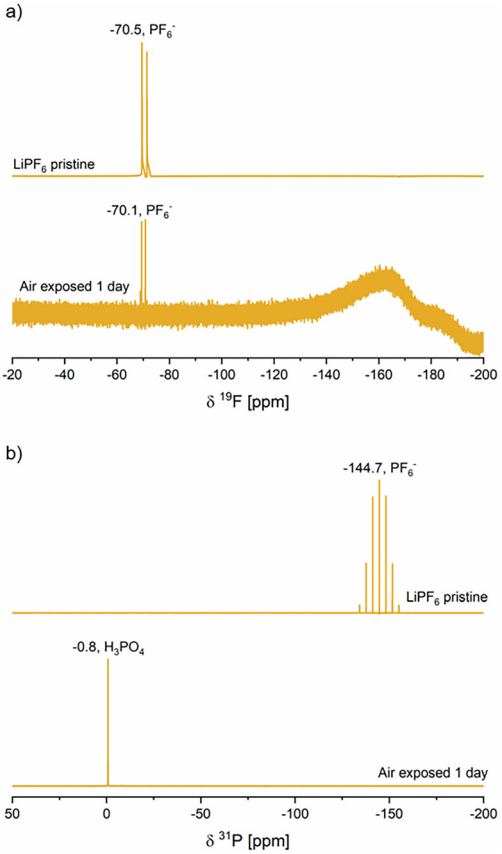

Fig. 3 (a) ^{19}F NMR (471 MHz, $(CD_3)_2SO$, 295 K) and (b) ^{31}P NMR (202 MHz, $(CD_3)_2SO$, 295 K) of pristine $LiPF_6$ and the soluble products after leaving 0.1 mmol $LiPF_6$ exposed to atmospheric air in an uncapped vial at room temperature (17–20 °C) for 1 day (24 hours).

NMR spectrum (Fig. 3b) showed no sign of the PF_6^- anion and instead a new singlet was seen at −0.8 ppm as the only signal.

The chemical shift of this new signal in the ^{31}P NMR spectrum indicates a P(V) species. The lack of ^{19}F–^{31}P coupling suggests that this is likely phosphoric acid, H_3PO_4, and this new signal matched the chemical shift of a separately prepared sample of phosphoric acid in DMSO-d_6 (Fig. S72). The formation of H_3PO_4 from the hydrolysis of $LiPF_6$ has previously been proposed,[35] and likely forms *via* a series of intermediate steps, generating POF_3, HPO_2F_2, H_2PO_3F and then H_3PO_4, along with HF.[36] However, we do not rule out the formation of a metal phosphate. In addition, insoluble material remained in the vial after the addition of DMSO-d_6, which is likely LiF (pristine $LiPF_6$ has good solubility in DMSO-d_6 solvent).

Thus, these NMR spectroscopic experiments show that $NaPF_6$ has a significantly higher tolerance to atmospheric air than $LiPF_6$. This finding is in agreement with previous reports on the rates of hydrolysis of $LiPF_6$ and $NaPF_6$ in solution.[36,37] Despite the high air stability of $NaPF_6$, reported studies have shown that $NaPF_6$ electrolytes are susceptible to hydrolysis in common battery solvents and hydrolysis is accelerated in the presence of protons.[12,36,37]

Previous studies on the rates of hydrolysis of 1 M XPF_6 (X = Li, Na and K) salts in solution have suggested that the Lewis acidity of the cation dictates the rate of decomposition of XPF_6, following the order $Li^+ > Na^+ > K^+$.[36,37] It is proposed that hydrolytic decomposition of XPF_6 follows a dissociative mechanism,[35] where the X^+ cation abstracts a fluoride from the PF_6^- anion, forming XF and PF_5. This proceeds *via* the proposed transition state in Scheme 1, as suggested in previous reports.[35,37] PF_5 then undergoes further decomposition and as evidenced in this work when using $LiPF_6$, the PF_6^- anion

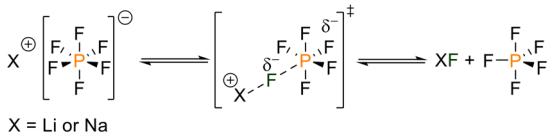

Scheme 1 Postulated decomposition mechanism of XPF_6 (X = Li or Na) into XF and PF_5. PF_5 then undergoes further decomposition.[35,37]

decomposes to form H_3PO_4 (along with likely LiF and HF) in atmospheric air. Interestingly, computational work has shown that under battery operating conditions, the interaction of PF_5 with lithium carbonate (a common solid-electrolyte interphase component in LIBs) may alter the rate of LiF and HF formation.[38] Nevertheless, the stronger Lewis acidity of Li^+ along with the greater lattice energy of LiF appear to be key factors in the poorer air tolerance of $LiPF_6$ compared to $NaPF_6$.

The structure of $NaPF_6$ coordinated to water, forming the monohydrate [$NaPF_6{\cdot}H_2O$], has previously been reported.[39,40] Thus, showing that $NaPF_6$ may form a hydrated structure in the presence of water. In our air exposure experiments, a strong intensity water signal was detected in the ^1H NMR spectra of the air exposed $NaPF_6$ samples (Fig. S61–S63), suggesting that [$NaPF_6{\cdot}H_2O$] formed when $NaPF_6$ was exposed to atmospheric air. The significant structural feature of [$NaPF_6{\cdot}H_2O$] is the presence of six-coordinate Na^+ cations, which are bonded to four equatorial F-atoms and two axial H_2O ligands. The structure of [$NaPF_6{\cdot}H_2O$] forms a complicated 3-D network which is propagated by extensive electrostatic Na···F and H-bonding H···F interactions, as shown in Fig. 4.[39,40] The ability of $NaPF_6$ to form a monohydrate structure has implications for its use as a battery electrolyte salt, as [$NaPF_6{\cdot}H_2O$] offers a source of water. Although $NaPF_6$ has been shown to have greater tolerance to air than $LiPF_6$, the presence of water in the electrolyte is problematic as under battery operating conditions, water can be oxidised to form H^+. The production of H^+ can accelerate the decomposition of PF_6^- in accordance to Scheme 1, where X = H.[35,37] Furthermore, the introduced water may participate in other degradation processes, for example the hydrolysis of ethylene carbonate and dimethylcarbonate.[41–43] Therefore, the ability to form [$NaPF_6{\cdot}H_2O$] highlights the importance of drying $NaPF_6$ before using it as a battery electrolyte salt.

Electrochemical comparisons of 1 M $NaPF_6$, 1 M NaTFSI and 1 M Na[B(hfip)$_4$]·DME in EC : DEC (1 : 1 v/v) were performed by firstly recording their bulk conductivities. Bulk conductivity is an important property as an electrolyte with high conductivity will enable rapid transport of Na^+ during charge/discharge cycles of the battery. Bulk conductivity measurements at 25 °C revealed 1 M $NaPF_6$ has the highest conductivity (8.6 mS cm^{-1}), followed by 1 M NaTFSI (6.6 mS cm^{-1}) and then 1 M Na[B(hfip)$_4$]·DME (5.1 mS cm^{-1}) (Fig. 5).

To investigate the bulk conductivities of 1 M $NaPF_6$, 1 M NaTFSI and 1 M Na[B(hfip)$_4$]·DME in EC : DEC (1 : 1 v/v) further, their conductivities were measured at the temperatures 25 °C, 35 °C, 45 °C and 55 °C (Fig. 5 and Table S1). For all electrolytes, the bulk conductivity increased with increasing temperature, with the 1 M $NaPF_6$ electrolyte having the highest conductivity at each given temperature. Consequently, the highest bulk conductivity recorded was for 1 M $NaPF_6$ at 55 °C (12.9 mS cm^{-1}). This compares to bulk conductivities of 10.1 mS cm^{-1} and 8.2 mS cm^{-1} for 1 M NaTFSI and 1 M Na[B(hfip)$_4$]·DME in EC : DEC at 55 °C, respectively. An Arrhenius plot of the electrolyte conductivity at different temperatures shows linear behaviour for all electrolytes across this temperature range. The gradient of this plot corresponds to the activation energy of the conduction process (activation energy required for the migration of ions) and when fitted to the Arrhenius equation, the activation energies are 10.8 kJ mol^{-1}, 11.6 kJ mol^{-1} and 12.7 kJ mol^{-1} for 1 M $NaPF_6$, 1 M NaTFSI and 1 M Na[B(hfip)$_4$]·DME electrolytes, respectively. Differences in ion solvation and viscosity will contribute to the differences in the activation energy.

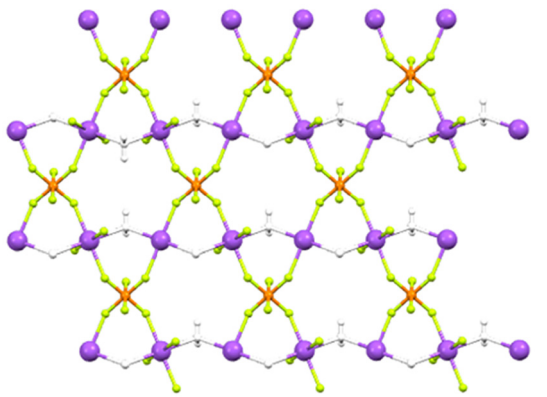

Fig. 4 Solid-state structure of $NaPF_6{\cdot}H_2O$, showing one layer of the 3D arrangement. Ball and stick model. White: water molecules, green: F, purple: Na, orange: P.

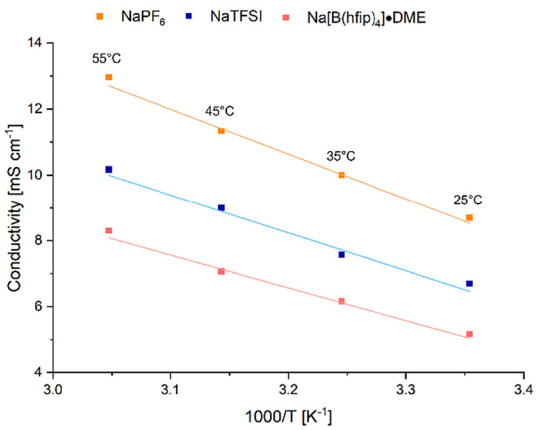

Fig. 5 Arrhenius plot of 1 M $NaPF_6$, 1 M NaTFSI and 1 M Na[B(hfip)$_4$]·DME in EC : DEC (1 : 1 v/v) solvent. Bulk conductivity measurements recorded at 25 °C, 35 °C, 45 °C and 55 °C. Electrolytes are 1 M $NaPF_6$ (orange), 1 M NaTFSI (blue) and 1 M Na[B(hfip)$_4$]·DME (pink) in EC : DEC (1 : 1 v/v).

The viscosity of an electrolyte is important as a highly viscous solution will hinder the mobility of ions, thus, an electrolyte with a low viscosity is desired to facilitate fast ion transport. Moreover, the viscosity of the electrolyte can impact the wetting of both the separator and electrodes in the battery. The viscosities of 1 M $NaPF_6$, 1 M NaTFSI and 1 M $Na[B(hfip)_4]$·DME in EC : DEC (1 : 1 v/v) electrolyte solutions were determined between 20 °C and 60 °C. As shown in Fig. 6, the viscosities of all three electrolyte solutions expectantly decrease with increased temperature. Therefore, the increase in bulk conductivity of the three electrolytes with increasing temperature can in part be explained by the decrease in solution viscosity.

At 20 °C, 1 M $Na[B(hfip)_4]$·DME exhibits the highest dynamic viscosity, 4.6 cP, which compares to 4.1 cP and 3.9 cP for 1 M $NaPF_6$ and 1 M NaTFSI, respectively. The higher viscosity for 1 M $NaPF_6$ over 1 M NaTFSI is consistent with previous findings using 1 M $NaPF_6$ and 1 M NaTFSI in EC : DMC solvent and 1 M $LiPF_6$ and 1 M LiTFSI in EC : DMC (1 : 1 wt%).[21,44] The lower viscosity for 1 M NaTFSI is likely due to differences in the degree of ion-pairing and Na^+ solvation shell. Interestingly, 1 M $Na[B(hfip)_4]$·DME showed the biggest decrease in viscosity with increasing temperature and the viscosities of all three electrolyte solutions had converged to 1.9 cP at 60 °C. Although 1 M $Na[B(hfip)_4]$·DME has the largest dynamic viscosity at 20 °C, likely due to the larger size of the $[B(hfip)_4]^-$ anion, at all temperatures the differences in the viscosity values are small and for practical applications indiscernible.

The electrochemical stability windows (ESWs) of 1 M $NaPF_6$, 1 M NaTFSI and 1 M $Na[B(hfip)_4]$·DME in EC : DEC (1 : 1 v/v) were determined using cyclic voltammetry (CV). A three-electrode cell with glassy carbon or aluminium foil as the working electrode was used; platinum was the counter electrode and sodium metal was the pseudo-reference. In all CV experiments, the current density of the oxidation waves decreased with increasing cycle number (for example, see Fig. S3).

When using glassy carbon as the working electrode, the current densities for 1 M NaTFSI were approximately a sixth lower than for 1 M $NaPF_6$ and an order of magnitude lower than for 1 M $Na[B(hfip)_4]$·DME, when measured at 5 V *vs.* Na/Na^+. Although the current densities cannot be directly compared, due to the difference in their bulk conductivities, the lower current densities when using 1 M NaTFSI cannot be explained by differences in the conductivities alone. By defining oxidation onset potential as occurring at a quarter of the maximum current density from the second cycle, for 1 M $NaPF_6$ in EC : DEC oxidation occurred at 4.8 V *vs.* Na/Na^+. This is slightly higher than for 1 M $Na[B(hfip)_4]$·DME in EC : DEC, 4.6 V *vs.* Na/Na^+ (Fig. 7).

When using a glassy carbon working electrode for 1 M NaTFSI in EC : DEC (1 : 1 v/v), the second cycle showed a peak centred at 4.5 V *vs.* Na/Na^+, as well as the bulk electrolyte oxidation peak. The peak at 4.5 V *vs.* Na/Na^+ does not appear on the first cycle and forms due to the reduction peak centred at 2.5 V *vs.* Na/Na^+ from the first cycle. This was confirmed by repeating the CV experiment but using 3 V as the lower cut-off voltage. By preventing the reduction process associated with the peak at 2.5 V *vs.* Na/Na^+, the oxidation peak at 4.5 V *vs.* Na/Na^+ was not observed (Fig. S6).

Further comment into the origin of the individual peaks in these cyclic voltammograms is beyond the scope of the current work. However, it has previously been shown when studying the oxidation of 1 M $LiPF_6$ in EC : DMC electrolyte on a glassy carbon electrode that oxidation of EC-related species occurs first, followed by oxidation of DMC-related species. A third oxidation process then takes place, which originates from the oxi-

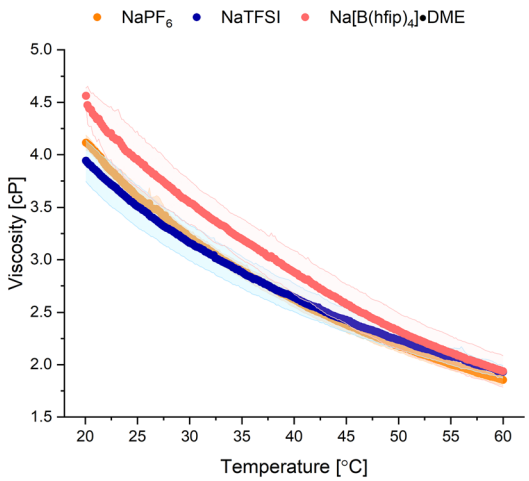

Fig. 6 Dynamic viscosity of 1 M $NaPF_6$ (orange), 1 M NaTFSI (blue) and 1 M $Na[B(hfip)_4]$·DME (pink) in EC : DEC (1 : 1 v/v) solvent. Error bars represent the standard deviation from three measurements. Arrhenius parameters (*A* and *B*) for $NaPF_6$ are *A* = 0.0051 mPa s, *B* = 1956.7 K, NaTFSI *A* = 0.0102 mPa s, *B* = 1739.7 K, $Na[B(hfip)_4]$·DME *A* = 0.0042 mPa s, *B* = 2040.9 K.

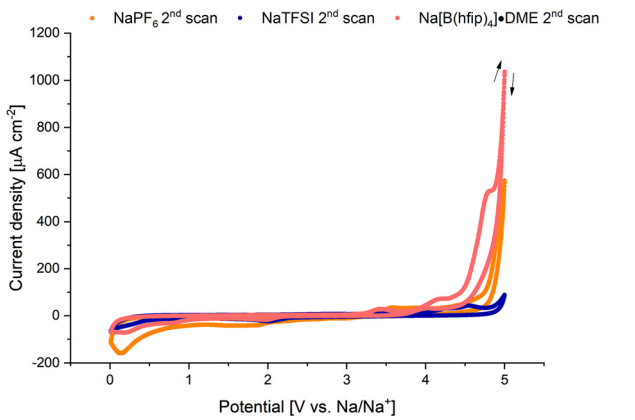

Fig. 7 Cyclic voltammetry of 1 M $NaPF_6$ (orange), 1 M NaTFSI (blue) and 1 M $Na[B(hfip)_4]$·DME (pink) in EC : DEC (1 : 1 v/v) in three-electrode cell. Working electrode: glassy carbon, counter electrode: platinum, reference electrode: sodium metal. 10 mV s^{-1} scan rate and 2nd cycle shown, measured between 0.01–5.0 V *vs.* Na/Na^+. Arrows show the direction of the CV experiment.

dation of EC- and DMC-related species, as well as from the oxidation of soluble products formed during the reduction of DMC-related species.[45] A separate study has investigated the oxidation of $LiPF_6$ in carbonate solvents using scanning electrochemical microscopy (SECM) and CV, using a glassy carbon electrode. This detected a reducible product at 3.15 V that is potentially associated with deprotonation of the carbonate solvents.[46] Fewer studies have investigated the oxidation and reduction mechanisms associated with LiTFSI-/NaTFSI-based electrolytes in carbonate solvents, but it has been shown using an inert platinum electrode that the anodic stability using a LiTFSI-based electrolyte increases with increasing LiTFSI concentration.[47]

CV experiments were then performed using aluminium as the working electrode, a common current collector for SIBs. For 1 M $NaPF_6$ and 1 M $Na[B(hfip)_4]$·DME in EC : DEC (1 : 1 v/v) (Fig. 8a), the appearance of the cyclic voltammograms were similar. Oxidation for the 1 M $Na[B(hfip)_4]$·DME electrolyte occurred at 3.5 V *vs.* Na/Na^+, whereas for 1 M $NaPF_6$ oxidation occurred at 3.3 V *vs.* Na/Na^+ (oxidation onset was deemed to occur at a quarter of the maximum current density, from the second cycle). Thus, $Na[B(hfip)_4]$·DME has greater oxidative stability towards aluminium, which is consistent with previous findings from the analogous $Li[B(hfip)_4]$·*x*DME (*x* = 2 or 3) salt.[30,48] Previous studies on aluminium using 1 M $Li[B(hfip)_4]$·3DME in EC : DMC as the electrolyte have revealed that AlF_3, Al_2O_3 and LiF form on the surface, likely caused by partial degradation of the $[B(hfip)_4]^-$ anion at high potentials.[30] These species form a stable passivating layer on aluminium which inhibits aluminium corrosion. As a result of this passivating layer, lower current densities were found using $Li[B(hfip)_4]$·3DME as the electrolyte salt compared to $LiPF_6$.[30]

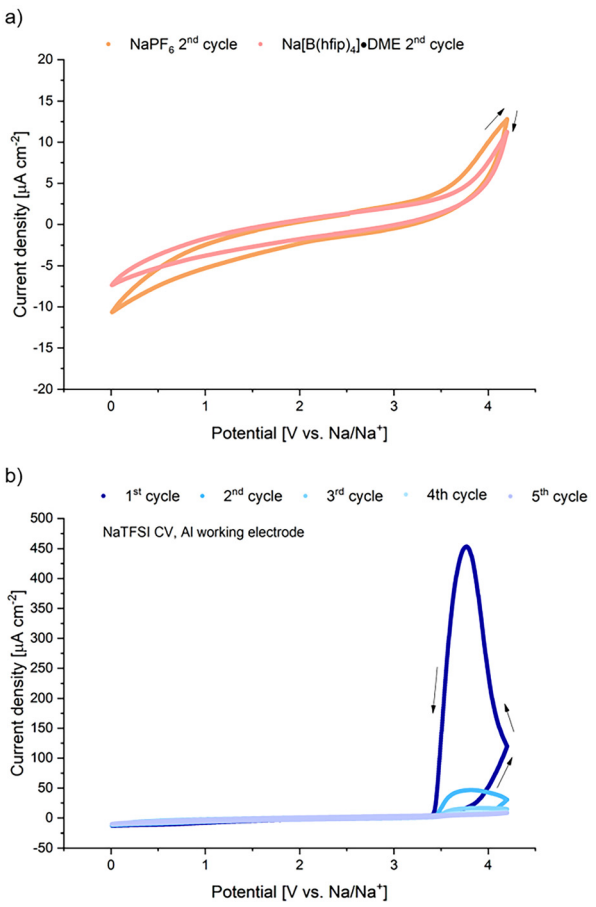

Fig. 8 (a) Cyclic voltammetry of 2nd cycle using 1 M $NaPF_6$ (orange) and 1 M $Na[B(hfip)_4]$·DME (pink) in EC : DEC (1 : 1 v/v) electrolyte in three-electrode cell. (b) Cyclic voltammetry of the first five cycles using 1 M NaTFSI (blue) in EC : DEC (1 : 1 v/v) electrolyte in three-electrode cell. Working electrode: aluminium, counter electrode: platinum, reference electrode: sodium metal. 5 mV s^{-1} scan rate measured between 0.01–4.2 V *vs.* Na/Na^+. Arrows show the direction of the CV experiment.

In contrast to 1 M $NaPF_6$ and 1 M $Na[B(hfip)_4]$·DME in EC : DEC (1 : 1 v/v), the appearance of the cyclic voltammogram of 1 M NaTFSI in EC : DEC was strikingly different when using aluminium as the working electrode (Fig. 8b). The current densities of the first cycle for 1 M NaTFSI were significantly larger than for 1 M $NaPF_6$ or 1 M $Na[B(hfip)_4]$·DME. Moreover, on the first cycle the current density continued to increase on reversal of the sweep direction, back towards lower potential, suggesting that the surface of the aluminium foil had changed. On the subsequent cycles, the current densities were an order of magnitude lower compared to the first cycle. This strongly indicated that corrosion of the aluminium foil had occurred.

The anodic dissolution of aluminium (aluminium corrosion) when using the fluorosulfonylimide (FSI^-) anion has been well studied for both LiFSI and NaFSI.[13–16] Mechanistic studies on the aluminium corrosion process have revealed that when an aluminium electrode is in contact with a non-aqueous electrolyte and is polarised in an anodic direction, Al^{3+} is formed. Initially, the formation of Al^{3+} is from Al_2O_3, which forms a protective surface layer. The high Lewis acidity of Al^{3+} results in it forming complexes with the solvent and the FSI^- anion (when using LiFSI or NaFSI), leading to aluminium corrosion. When using $LiPF_6$ or $NaPF_6$ as the electrolyte salt, a passivating AlF_3 film on the surface of the aluminium electrode forms, due to the reaction of HF (formed from the hydrolysis of $LiPF_6$ or $NaPF_6$) with Al_2O_3, which suppresses aluminium corrosion.[13,14] Thus, highlighting that a small quantity of HF can be beneficial to form a protecting surface to prevent aluminium corrosion.

To confirm if aluminium corrosion was the cause of the large current densities when using 1 M NaTFSI in EC : DEC (1 : 1 v/v), scanning electron microscopy (SEM) images of the aluminium foil after the CV experiment were taken (Fig. 9). The resulting SEM images confirmed the presence of pitting on the aluminium surface, which were found to nucleate along the lines of the aluminium foil left from the manufacturing process. Furthermore, images of the aluminium pitting were taken with a digital microscope and revealed that the pitting was approximately 0.2–1 μm in depth and approximately 3–5 μm in diameter (Fig. S46). Thus, this CV experiment confirms that 1 M NaTFSI in EC : DEC is not a compatible electro-

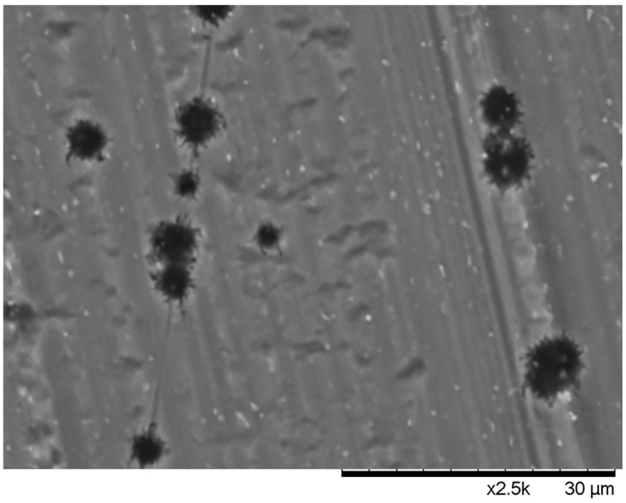

Fig. 9 SEM surface image of the aluminium working electrode that was used in the cyclic voltammetry experiment using 1 M NaTFSI in EC : DEC electrolyte, measured between 0.01–4.2 V *vs.* Na/Na^+.

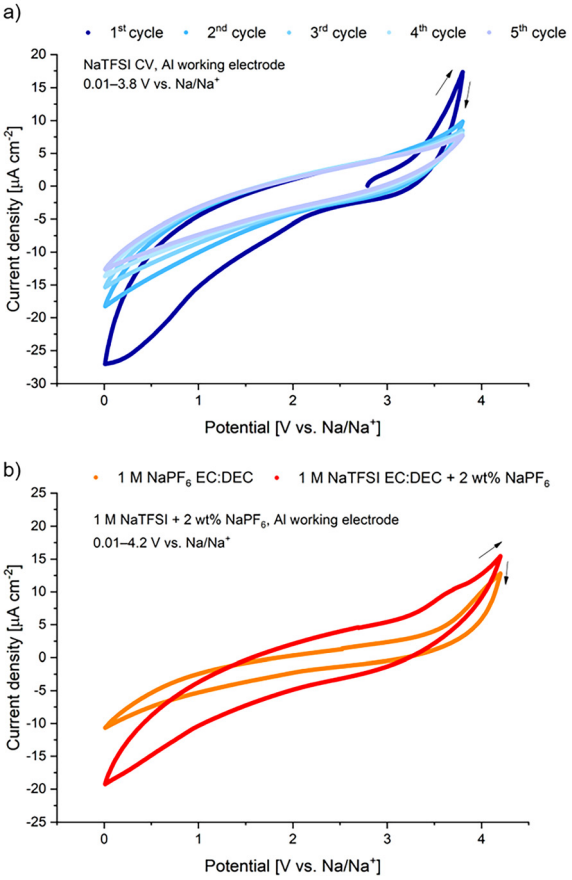

Fig. 10 Cyclic voltammetry of (a) 1 M NaTFSI in EC : DEC (1 : 1 v/v) in three-electrode cell, measured between 0.01–3.8 V *vs.* Na/Na^+. (b) Cyclic voltammetry of 1 M $NaPF_6$ in EC : DEC (1 : 1 v/v) (orange) and 1 M NaTFSI in EC : DEC (1 : 1 v/v) + 2 wt% $NaPF_6$ (red) in three-electrode cell, measured between 0.01–4.2 V *vs.* Na/Na^+, showing the 2nd cycle. Working electrode: aluminium, counter electrode: platinum, reference electrode: sodium metal. 5 mV s^{-1} scan rate. Arrows show the direction of the CV experiment.

lyte for use with high-voltage cathodes using an aluminium current collector.

To investigate whether aluminium corrosion could be supressed when using 1 M NaTFSI in EC : DEC as the electrolyte, the CV experiment was repeated, with the upper cut-off voltage lowered to 3.8 V *vs.* Na/Na^+ (Fig. 10a). In this case, the appearance of the cyclic voltammogram was comparable to using 1 M $NaPF_6$ and 1 M $Na[B(hfip)_4]$·DME in EC : DEC as electrolyte solutions. Moreover, significantly lower current densities were observed than when cycled at 4.2 V *vs.* Na/Na^+, which suggested that corrosion of the aluminium working electrode had not taken place. This was confirmed by taking SEM images of the aluminium foil after the CV experiment, which did not show pitting or signs of corrosion (Fig. S40–S41).

Considering that most cathode materials used for SIBs, including some PBAs, use upper cut-off voltages above 3.8 V, $NaPF_6$ was added as an additive to 1 M NaTFSI in EC : DEC (1 : 1 v/v) to investigate whether it would suppress aluminium corrosion. The CV of a 1 M NaTFSI in EC : DEC (1 : 1 v/v) with 2 wt% $NaPF_6$ added was measured using aluminium as the working electrode and with an upper cut-off voltage of 4.2 V *vs.* Na/Na^+. The current densities were significantly lower than using 1 M NaTFSI alone. Moreover, the appearance of the cyclic voltammogram was similar to using 1 M $NaPF_6$ in EC : DEC (Fig. 10b). This indicated that corrosion of the aluminium foil had not occurred, which was confirmed by SEM images of the post-cycled aluminium foil (Fig. S42 and S43).

Having understood the fundamental properties of the $NaPF_6$, NaTFSI and $Na[B(hfip)_4]$·DME electrolyte salts, their performance in SIBs was investigated. For this, coin cells were assembled using a Prussian white, $Na_2Fe[Fe(CN)_6]$, cathode and either a sodium metal or hard carbon anode. The electrolytes tested were 1 M $NaPF_6$, 1 M NaTFSI and 1 M $Na[B(hfip)_4]$·DME in EC : DEC (1 : 1 v/v). For the half-cells containing a Prussian white cathode and sodium metal electrode, 1 M $Na[B(hfip)_4]$·DME gave the most stable cycling, but in all cases the capacity retention was low (Fig. S13). This is likely due to the incompatibility of the carbonate solvent with sodium metal.[49]

For the Prussian white *vs.* hard carbon full-cell cycling, the cycling protocol involved two C/20 rate formation cycles, followed by 300 1C rate cycles and two C/20 rate cycles to end. This set of 304 cycles was then repeated to give a total of 608 cycles. Cell voltage limits of 1.5–3.8 V were used during the extended charge/discharge cycles and the capacity ratio of anode to cathode is approximately 1.3 : 1.

Throughout the 608 cycles, the 1 M $NaPF_6$ and 1 M NaTFSI in EC : DEC electrolyte gave stable cycling, performing comparably with respect to initial capacity, capacity retention and coulombic efficiency (Fig. 11a and S15). The discharge voltage profiles, shown in Fig. 11b and S16–S18, are similar throughout

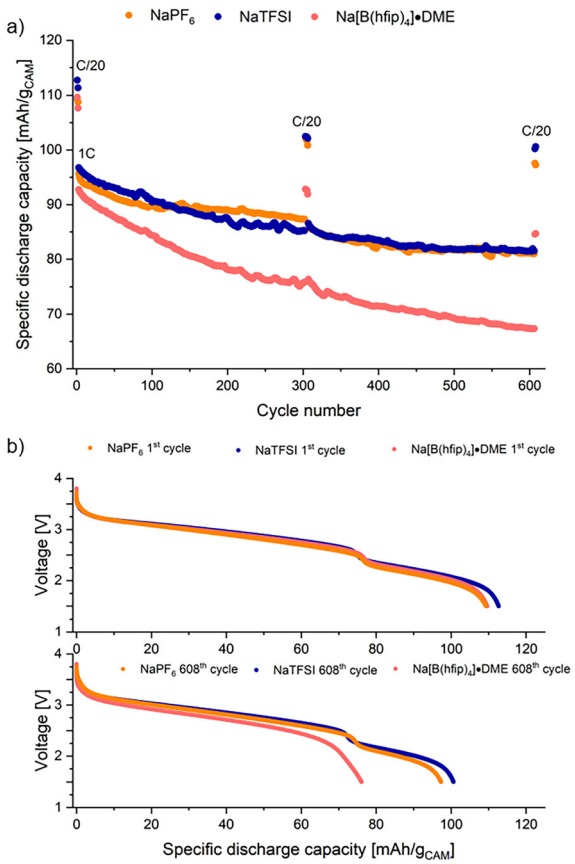

Fig. 11 (a) Specific discharge capacity *vs.* cycle number. (b) Voltage *vs.* specific discharge capacity for the 1st and last (608th) C/20 cycle. Cycling from coin cells using a Prussian white cathode and hard carbon anode. The applied C-rates of C/20 and 1C were calculated based on the theoretical capacity of 150 mA h g^{-1} of the cathode, using cell voltage limits of 1.5 and 3.8 V. Electrolytes are 1 M $NaPF_6$ (orange), 1 M NaTFSI (blue) and 1 M Na[B(hfip)$_4$]·DME (pink) in EC : DEC (1 : 1 v/v). Cells cycled at 21 °C. Note the 1st discharge voltage profiles of Na[B(hfip)$_4$]·DME and $NaPF_6$ are similar which obscures Na[B(hfip)$_4$]·DME in b, top.

the 608 cycles. From the first C/20 rate formation cycle, the cells began with approximately 110 mA h g^{-1} capacity, which decreased to approximately 95 mA h g^{-1} for the first 1C cycle. The capacities for the final 1C cycles were 81 mA h g^{-1} and 82 mA h g^{-1} for 1 M $NaPF_6$ and 1 M NaTFSI, respectively. The capacity retentions for 1 M $NaPF_6$ and 1 M NaTFSI electrolytes were 85% and 84%, respectively, as determined from the first and last 1C rate cycles. Both the $NaPF_6$- and NaTFSI-containing electrolytes took until the 4th cycle to reach 99% coulombic efficiency, which was then maintained throughout the remaining charge/discharge cycles. Thus, these cycling results show that when using a Prussian white cathode, 1 M NaTFSI in EC : DEC is a viable alternative to using 1 M $NaPF_6$ in EC : DEC, as both electrolytes provide stable long-term cycling, even at moderately high rate.

In contrast, the 1 M Na[B(hfip)$_4$]·DME in EC : DEC electrolyte performed more poorly. After the formation cycles the Na[B(hfip)$_4$]·DME electrolyte started with a slightly lower initial capacity and gave a lower capacity retention of 73% after 608 cycles; determined using the first and last 1C cycles (Fig. 11a). This greater capacity loss occurred early during cycling, as seen by the C/20 rate diagnostic signals after 304 cycles.

The poorer capacity retention observed when using 1 M Na[B(hfip)$_4$]·DME in EC : DEC electrolyte corresponds with loss of the lower discharge plateau, unlike with the 1 M $NaPF_6$ and 1 M NaTFSI electrolytes which retain this plateau throughout (Fig. 11b and S16–S18). This lower plateau occurs due to a phase transition between cubic and rhombohedral phases in the Prussian white cathode during cycling. Previous studies examining capacity fade using Prussian white cathodes found that most of the capacity is lost from this lower potential plateau.[50,51] The loss of the lower plateau in this work indicates sodium inventory loss.[50] In addition, the detrimental role of DME may in part explain the capacity loss, as has previously been observed when comparing the cycling performance of solvated Li[Al(hfip)$_4$]·DME and unsolvated Li[Al(hfip)$_4$] in $LiNi_{0.8}Mn_{0.1}Co_{0.1}O_2$ (NMC811) *vs.* graphite cells.[48] Nevertheless, the coulombic efficiencies of the 1 M Na[B(hfip)$_4$]·DME electrolyte were comparable to the 1 M $NaPF_6$ and 1 M NaTFSI electrolytes.

The solid-electrolyte interphase (SEI, at the anode) and cathode-electrolyte interphase (CEI, at the cathode) are essential for long-term stable cycling. These interphases form on the initial cycle and are produced by the interaction between the electrolyte and electrode. Once formed, these interphases act as a passivating layer which can prevent further electrolyte and electrode decomposition.[52,53] To understand the nature and composition of the SEI and CEI formed from the cell cycling using 1 M $NaPF_6$, 1 M NaTFSI and 1 M Na[B(hfip)$_4$]·DME in EC : DEC electrolytes, X-ray photoelectron spectroscopy (XPS) measurements on the post-cycled Prussian white cathode and hard carbon anode were taken (see SI Fig. S19–S35 for complete XPS spectra).

Previous degradation studies on Prussian white cathodes have revealed that irreversible structural decomposition occurs under basic conditions.[54] The reduction of water leads to the formation of H_2 and OH^-, which participates in the ring opening of EC and results in the evolution of CO_2. Hydroxides then react with CO_2 to form sodium carbonate.[55] Cyanogen, $(CN)_2$, release from the Prussian white cathode is known to occur during overcharge, which is hypothesised to form due to the reductive elimination of cyanide-coordinated Fe^{4+} intermediate.[56] This in turn leads to surface reorganisation, where a layer containing $Fe[Fe(CN)_4][Y]_2$ (Y = negatively charged ligand from the electrolyte) is formed.[55]

XPS measurements of the post-cycled hard carbon anode revealed decomposition of the electrolyte occurred during the 608 cycles. As all three electrolyte salts contain fluorine, the F 1s spectrum was used to analyse degradation of the salts (Fig. 12a). Using 1 M $NaPF_6$ in EC : DEC as the electrolyte, the F 1s XPS spectrum of the post-cycled hard carbon showed a P–F peak at a binding energy of 688.7 eV, which is from residual $NaPF_6$ and/or degradation of the PF_6^- anion, *e.g.* POF_3. In

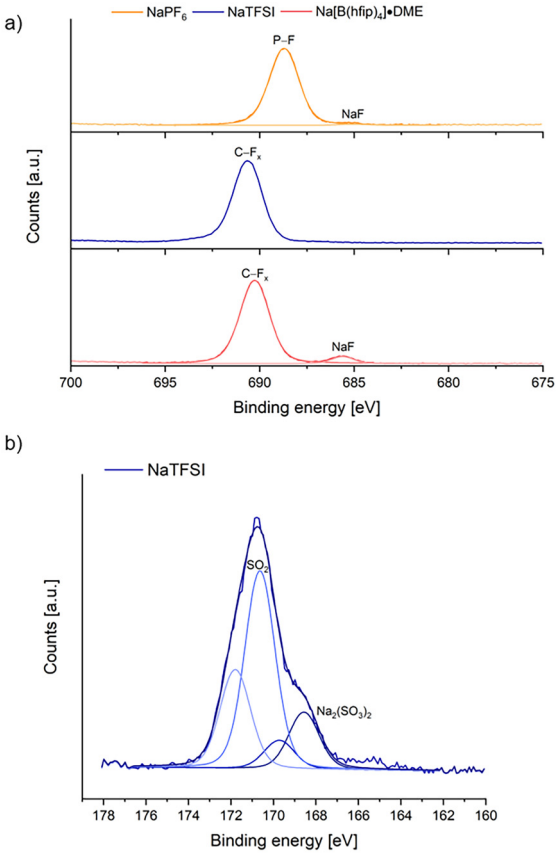

Fig. 12 (a) F 1s XPS spectra of post-cycled hard carbon anode using 1 M $NaPF_6$ (orange), 1 M NaTFSI (blue) and 1 M $Na[B(hfip)_4]$·DME (pink) in EC : DEC (1 : 1 v/v) as the electrolytes. (b) S 2p XPS spectrum of post-cycled hard carbon anode using 1 M NaTFSI in EC : DEC (1 : 1 v/v) as the electrolyte.

addition, a low-intensity peak at 685.0 eV was observed, which is assigned to NaF. Using 1 M NaTFSI as the electrolyte, the F 1s spectrum revealed only one peak at 690.7 eV, corresponding to C–F_x, either from residual salt and/or partial decomposition of the $TFSI^-$ anion. In this work, no NaF peak was observed for NaTFSI in the F 1s XPS spectrum, but NaF has been reported to form on the hard carbon in other studies.[57] For the 1 M $Na[B(hfip)_4]$·DME electrolyte, the F 1s spectrum showed two peaks at 690.3 eV and 685.6 eV, which are assigned to C–F_x (either residual salt and/or salt decomposition) and NaF, respectively. As determined from the surface concentrations of species present at *ca.* 685 eV (assigned to NaF) in the F 1s XPS spectrum, there was approximately six times greater concentration of NaF on the post-cycled anode when using $Na[B(hfip)_4]$·DME than $NaPF_6$ as the electrolyte salt.

For the 1 M NaTFSI electrolyte, the S 2p XPS spectrum showed $Na_2(SO_3)_2$ at 168.6 eV (S $2p_{3/2}$ peak), as well as an SO_2 group (either from residual NaTFSI or decomposed salt) at 170.6 eV (S $2p_{3/2}$ peak, Fig. 12b). The SO_2 group is at a higher-than-expected binding energy due to the electron withdrawing nature of the $-CF_3$ group attached. This is consistent with previous findings.[58] Moreover, the Al 2p XPS spectrum from the NaTFSI sample showed a peak at 76.5 eV, corresponding to Al^{3+} (Fig. 13a).[59] Neither the post-cycled anodes using 1 M $NaPF_6$ or 1 M $Na[B(hfip)_4]$·DME electrolyte showed this Al^{3+} peak and it is hypothesised that this is a result of aluminium corrosion processes during battery cycling.

The pristine hard carbon anode has a peak at 284.4 eV in the C 1s XPS spectrum, characteristic of hard carbon. For the post-cycled anodes, this peak significantly decreases in intensity, irrespective of the electrolyte used, indicating the formation of an SEI layer (Fig. 13b).[60] The post-cycled anodes show additional peaks compared to the pristine sample, which is a result of solvent breakdown. This is also evidenced in the O 1s XPS spectra (Fig. S29). From the atomic ratios, the oxygen concentration in the SEI was greatest when using NaTFSI as the electrolyte salt (32.8%), compared to $NaPF_6$ (24.3%) and $Na[B(hfip)_4]$·DME (27.7%). A carbonate group (CO_3^{2-}) is observed in all three samples at *ca.* 289 eV, which may be assigned to Na_2CO_3. However, it has previously been reported in sodium metal *vs.* hard carbon cells that sodium ethylene dicarbonate (NEDC, $NaO_2CO–C_2H_4–OCO_2Na$), which forms from the reduction of ethylene carbonate, is the dominant carbonaceous species when using either 1 M $NaPF_6$ or 1 M NaTFSI in EC : DMC.[57] Therefore, NEDC may be the dominant carbonaceous species in this work. None of the hard carbon

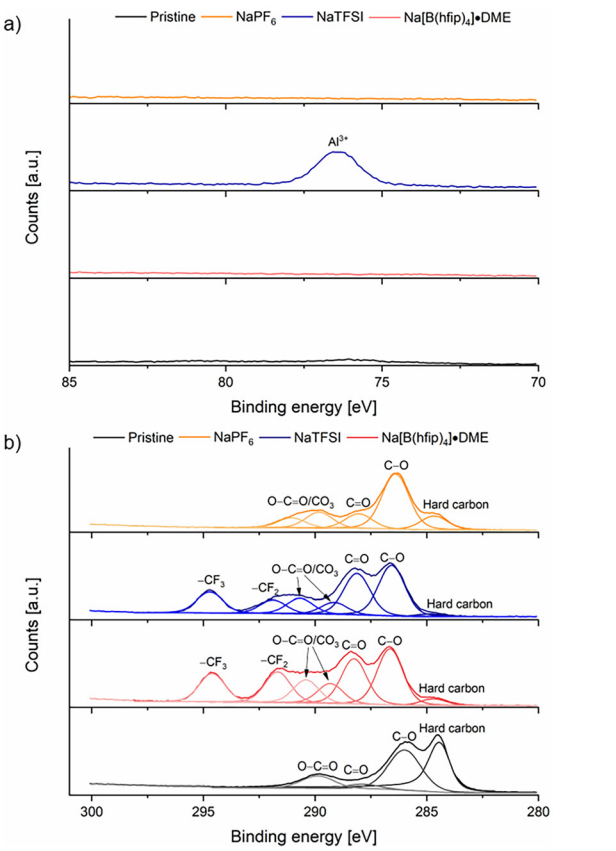

Fig. 13 (a) Al 2p XPS spectrum and (b) C 1s XPS spectrum of post-cycled hard carbon anode using 1 M $NaPF_6$ (orange), 1 M NaTFSI (blue) and 1 M $Na[B(hfip)_4]$·DME (pink) in EC : DEC (1 : 1 v/v) as the electrolytes.

anode samples showed iron present in the Fe 2p spectra, thus indicating that iron dissolution (which would have migrated from the cathode, travelled through the liquid electrolyte and deposited on the anode) had not occurred during cycling. Although there were no signs of iron present in the XPS spectra of our hard carbon samples, iron has been detected using inductively coupled plasma optical emission spectroscopy (ICP-OES) on post-cycled hard carbon electrodes from cell cycling using a sodium manganese hexacyanoferrate $Na_2Mn[Fe(CN)_6]$ (NaMnHCF) cathode.[61]

XPS measurements were taken on the post-cycled Prussian white cathodes to determine the nature of the CEI. The F 1s XPS spectrum showed one peak for both the post-cycled cathodes using 1 M $NaPF_6$ and 1 M NaTFSI in EC : DEC electrolytes, corresponding to P–F (686.7 eV) and C–F_x (689.1 eV), respectively. In contrast, the post-cycled cathode with 1 M Na[B(hfip)$_4$]·DME electrolyte showed two peaks at 688.7 eV and 684.6 eV (Fig. 14a). The former is due to a C–F_x group while the latter is assigned to NaF. The cathode using 1 M NaTFSI electrolyte showed similar findings to the hard carbon anode, with the S 2p XPS spectrum showing $Na_2(SO_3)_2$ at 169.2 eV (S $2p_{3/2}$ peak), and the Al 2p spectrum displaying a peak at 75.0 eV, which is assigned to Al^{3+}. In addition, the C 1s (Fig. 14b) and O 1s (Fig. S20) XPS spectra revealed solvent breakdown. The Fe 2p spectra did not show evidence of surface reorganisation to $Fe[Fe(CN)_4][Y]_2$, as previously reported.[61]

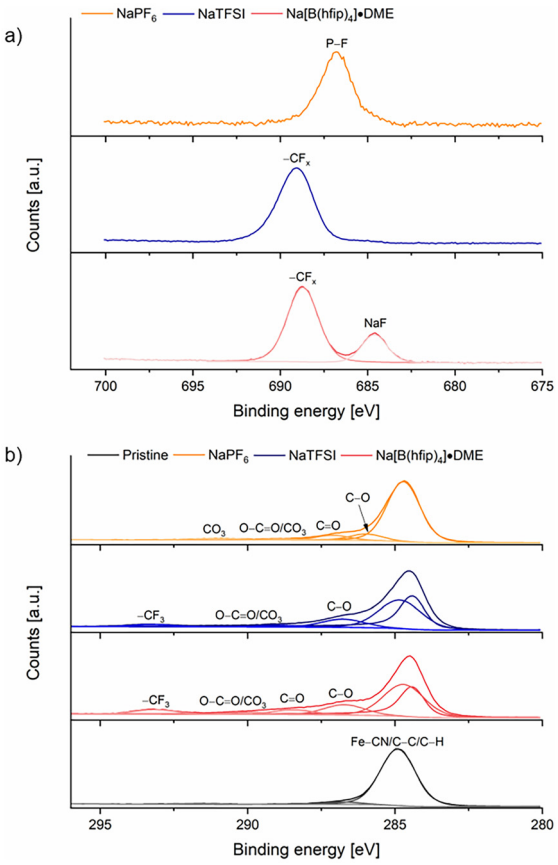

Fig. 14 (a) F 1s and (b) C 1s XPS spectra of post-cycled Prussian white cathode using 1 M $NaPF_6$ (orange), 1 M NaTFSI (blue) and 1 M Na[B(hfip)$_4$]·DME (pink) in EC : DEC (1 : 1 v/v) as the electrolytes.

The thickness of the CEI was estimated using the iron signal attenuation (without the topographical correction factor),[62] which showed a thinner CEI is formed when using NaTFSI as the electrolyte salt (*ca.* 0.3 nm). This compares to estimated CEI thicknesses of *ca.* 1.6 nm and *ca.* 2.6 nm when using $NaPF_6$ and Na[B(hfip)$_4$]·DME as the electrolyte salts, respectively. The thicker CEI formed for cells containing Na[B(hfip)$_4$]·DME may in part explain the lower initial capacity and poorer capacity retention for cycling. Interestingly, from the atomic ratios the CEI formed from using Na[B(hfip)$_4$]·DME as the electrolyte salt contained a greater concentration of sodium (10.6%) and fluorine (17.7%) than when using NaTFSI (4.1% and 10.4%, respectively), which in turn had a greater percentage of sodium and fluorine in its CEI than $NaPF_6$ (1.0% and 2.9%, respectively).

Lastly, as the electrolyte 1 M NaTFSI + 2 wt% $NaPF_6$ in EC : DEC (1 : 1 v/v) was found to limit aluminium corrosion in the CV experiments, coin cells were assembled using this electrolyte and tested in galvanostatic cycling (Fig. 15a). A Prussian white cathode and hard carbon anode were again used and the cycling procedure involved one C/25 rate formation cycle at room temperature (21 °C), followed by cycling at C/2 rate at 40 °C, 50 °C and then 60 °C. By cycling at elevated temperatures, the suitability of using this electrolyte for high-temperature applications could be determined. An electrolyte that performs well at high temperatures is beneficial as it negates the need for expensive cooling systems, which for example is important for countries which do not have a temperate climate, such as sub-Saharan Africa.

The electrolyte 1 M NaTFSI + 2 wt% $NaPF_6$ in EC : DEC cycled with an initial specific discharge capacity of 126 mA h g^{-1}. When proceeding with cycling at 40 °C at C/2 rate, stable cycling was observed throughout the 102-cycle duration. The first C/2 rate cycle at 40 °C began with a specific discharge capacity of 119 mAh g^{-1} and had a capacity retention of 82% (determined from the first and last C/2 rate cycle at 40 °C). Following this, the temperature was increased to 50 °C, where stable cycling was still seen and after 116 cycles at 50 °C the capacity retention was 89% (determined from the first and last cycle at 50 °C). A further increase in the temperature to 60 °C continued to give stable cycling and after 81 cycles at this temperature the capacity retention was 93% (determined from the first and last cycle at 60 °C). Over the course of the 299 C/2 rate cycles the capacity retention was 76%.

The variable temperature cycling results using 1 M NaTFSI + 2 wt% $NaPF_6$ in EC : DEC (1 : 1 v/v) show that this is a promising electrolyte for applications in high-temperature SIBs. Although the capacity retention was lower for this electrolyte at elevated temperatures compared to using 1 M NaTFSI in EC : DEC at 21 °C, this is likely a result of accelerated electrolyte degradation and dissolution of thermally unstable components in the SEI at higher temperatures. The voltage *vs.* specific capacity plots have been compared for the 50th, 150th

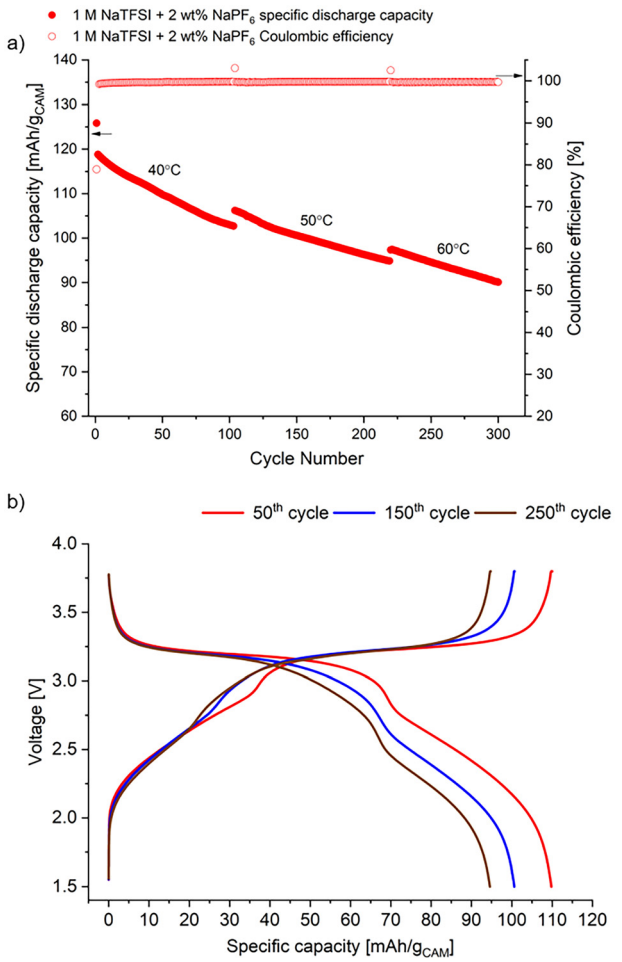

Fig. 15 (a) specific discharge capacity *vs.* cycle number (filled circles) and coulombic efficiency *vs.* cycle number (non-filled circles). (b) Voltage *vs.* specific capacity for the 50th (red), 150th (blue) and 250th (brown) cycles. Cycling from coin cells using a Prussian white cathode and hard carbon anode. The applied C-rates of C/25 and C/2 were calculated based on the theoretical capacity of 150 mA h g^{-1} of the cathode, using cell voltage limits of 1.5 and 3.8 V. Electrolyte is 1 M NaTFSI + 2 wt% $NaPF_6$ in EC : DEC (1 : 1 v/v). Cells cycling at 40 °C, 50 °C and 60 °C.

and 250th cycles, which shows retention of the lower discharge plateau throughout the cell cycling (Fig. 15b).

Conclusions

In conclusion, this work has investigated the use of NaTFSI and Na[B(hfip)$_4$]·DME as alternative electrolyte salts to the current benchmark $NaPF_6$ and assessed their application for SIBs. The air stability of the three salts was investigated and it was found using solution-state multinuclear NMR spectroscopy that both $NaPF_6$ and NaTFSI were highly stable to atmospheric air after one month. In contrast, Na[B(hfip)$_4$]·DME underwent partial decomposition. The air stability of $NaPF_6$ was compared to $LiPF_6$, where in contrast to the former $LiPF_6$ fully decomposed after 24 hours to give H_3PO_4 (and likely LiF and HF). The higher Lewis acidity of Li^+ and greater lattice enthalpy of LiF are suggested as key contributing factors to the differences in the air stability between $NaPF_6$ and $LiPF_6$.

Electrochemical investigations found that 1 M $NaPF_6$ in EC : DEC has the highest bulk conductivity and is compatible with aluminium foils. In contrast, from CV experiments aluminium corrosion occurred when using 1 M NaTFSI in EC : DEC when cycled to 4.2 V *vs.* Na/Na^+. Corrosion can be supressed by either cycling at lower voltages or by the addition of 2 wt% $NaPF_6$ as an electrolyte additive. Nevertheless, 1 M NaTFSI gave stable extended charge/discharge cycling in coin cells employing a Prussian white cathode and hard carbon anode at moderately high rate (1C), which was similar to using 1 M $NaPF_6$ in EC : DEC with respect to initial capacity and capacity retention. Thus, these cycling results show that NaTFSI is a viable alternative electrolyte salt to using $NaPF_6$ in cells using a Prussian white cathode and offers a potentially safer electrolyte choice due to the lower likelihood of toxic HF generation (on account of the strong C–F bonds in NaTFSI).

Experimental

Anhydrous THF and 1,2-dimethoxyethane (DME) were purchased from Merck U.K. and used as received. Deuterated solvents were dried over 4 Å activated molecular sieves and stored in an argon filled glovebox. Sodium bis(trifluoromethylsulfonyl)imide (battery grade) was purchased from Solvionic and used as received. $NaPF_6$ and Na[B(hfip)$_4$]·DME electrolyte salts were prepared using previous literature methods.[29,63] ^{1}H, ^{13}C{^{1}H}, ^{19}F, ^{11}B and ^{31}P solution-state NMR spectra were recorded at 298.0 K on a Bruker 500 MHz AVIII HD Smart Probe spectrometer. Chemical shifts are expressed as parts per million (ppm, δ) and are referenced to CD_3CN (1.95/118.26 ppm) and $(CD_3)_2SO$ (2.50/39.52 ppm) as internal standards. Multinuclear NMR spectra were referenced to $BF_3{\cdot}Et_2O$/$CDCl_3$ (^{11}B), $CFCl_3$ (^{19}F) and H_3PO4 (^{31}P). The description of signals includes s = singlet, d = doublet, t = triplet, q = quartet, q = quintet and m = multiplet. All coupling constants are absolute values and are expressed in Hertz (Hz).

Ethylene carbonate: diethyl carbonate (EC : DEC 1 : 1 v/v) was prepared by weighing a known amount of EC and translating this to a volume using the density 1.321 g mL^{-1}. The equal volume of DEC was added; gentle heating to 50 °C was required to fully dissolve EC. The 1 : 1 by volume ratio was confirmed by integrating the EC and DEC signals in the ^{1}H NMR spectrum. The prepared solvent was degassed using freeze–pump–thaw degas technique and dried over 4 Å activated molecular sieves to *ca.* 10 ppm water (determined by Karl-Fischer titration).

Solution ionic conductivity measurements were performed using an in-house designed two-electrode platinum cell (see Fig. S1). 2 ml of each electrolyte was filled into the cell and the rubber septum was sealed with parafilm to prevent air/moist-

ure exposure. Impedance spectra were measured using an Ivium potentiostat with an applied voltage amplitude of 25 mV and frequencies between 10 kHz and 0.1 Hz. The temperature was kept constant by submerging the electrolyte solution in a silicon oil bath at fixed temperature. For the electrolyte solutions, impedance spectra were recorded at 25 °C, 35 °C, 45 °C and 55 °C and fitted using the circuit $R + Q$. The solution conductivity was found by taking the reciprocal of the R component, multiplied by the cell constant (see SI).

Viscosity measurements were performed using a TA Instruments HR30 rheometer fitted with a 60 mm diameter hard anodised aluminium parallel plate geometry at a geometry gap of 400 μm. Temperature control was achieved using a lower Peltier plate geometry. Evaporation was controlled using a solvent trap. Temperature ramps (20 °C to 60 °C at a ramp rate of 0.5 °C min^{-1}) were performed in triplicate. Preliminary shear rate sweeps were performed to confirm that the sample behaved as Newtonian fluids (and hence could be characterised using a single, constant, viscosity parameter, μ). Data, $\mu(T)$ (as shown in Fig. 6) was fitted to an Arrhenius type model [$\mu = A\exp(-B/T)$] and the parameters A (Pa.s) and B (K) are shown in the legend of Fig. 6.

The studied electrolytes' electrochemical stability window (ESW) was determined using cyclic voltammetry (CV). Solutions of 1 M electrolyte in EC : DEC (1 : 1 v/v) were tested in three-electrode cells (in house designed) using either glassy carbon or battery-grade aluminium as the working electrode (WE). Platinum and sodium were used as the counter electrode and pseudo reference electrode, respectively. The three-electrode cell is a "beaker style" cell that uses an excess of electrolyte (2 ml) and does not use a separator. Each CV experiment comprised of five consecutive CV scans, at either 10 mV s^{-1} or 5 mV s^{-1}, for the glassy carbon and aluminium working electrode, respectively.

Optical imagery and 3d spatial data were obtained by mounting samples on a levelling sample holder and imaging with a Keyence VHX 7100 Digital microscope, VHX s7503 motorised stage and VHX imaging software version 1.4.23.17. Full 3d spatial data was obtained using serial recording and 3d dimensional image stitching within the VHX software application to produce 3d representations where measurements of depth and diameter were obtained.

Electron microscopy was performed using a Hitachi TM3030Plus tabletop microscope with an Oxford Instruments EDS X-stream-2 and MicsF+. Images were captured using the TM3030 software version 01-05-02, with additional images captured and EDX spectra obtained and analysed with AztecOne Sp1 3.1 software.

Prussian white was synthesised using an adapted two-step method.[64,65] Prussian blue (PB) was synthesised from $Na_4Fe(CN)_6{\cdot}10H_2O$ and ascorbic acid in 0.1 M HCl, gradually heated to 80 °C and stirred for 4 hours to form high-quality crystals. The product was centrifuged and washed repeatedly with ethanol–water (1 : 1 v/v). Prussian white was obtained by reducing the PB suspension with stoichiometric $NaBH_4$ for 30 minutes under ambient conditions. The resulting Prussian white was washed with ethanol and thoroughly dried under heat–vacuum (170 °C, 2×10^{-2} mbar, 20 hours) to remove residual moisture and minimise oxidation. Resulting rhombohedral Prussian white powder was stored in an argon filled glove box to avoid oxidation. The electrodes were prepared by mixing Prussian white powder, Super-P® carbon black, carboxymethylcellulose (CMC, MW = 90 000) and styrene–butadiene rubber (SBR) to form a slurry. The ratios were respectively 80 : 10 : 3 : 7 wt%. Deionised water was used as solvent. The components were mixed in Thinky mixer (THINKY ARE-250) in steps, starting with dissolving CMC in water, then adding carbon black, then active material and finally SBR binder. The slurry was coated on 15 μm aluminium foil (battery-grade MTI) using an automatic film coater (MSK-AFA-II-VC-FH-MTI) and doctor blade and subsequently dried at 170 °C at $\times 10^{-3}$ mbar for 24 hours before being transferred to the glovebox for use in a cell. The negative electrode was prepared in similar way using a commercially available hard carbon from Batri Ltd (Wales, U.K.). The ratios were 80 : 10 : 10 wt% for hard carbon, Super P and CMC binder respectively. The electrodes were dried at 100 °C at $\times 10^{-2}$ mbar for 24 hours.

Coin cells (2032 from Cambridge energy solutions) were prepared in an argon glovebox (MBraun, O_2 < 5 ppm, H_2O < 1 ppm). For Na-ion coin cells, a Prussian white, $Na_2Fe[Fe(CN)_6]$, cathode of area 1.33 cm^2 was assembled with a geometrically over-sized hard carbon anode (1.54 cm^2). The n : p ratio was approximately 1.3 : 1. Glass fibre was used as the separator, which was dried at 80 °C under vacuum for 48 hours prior to using; 100 μl of electrolyte was added to the separator.

The electrochemically cycled Prussian white and hard carbon electrodes underwent rinsing with diethyl carbonate (DEC) solvent and were subsequently dried for X-ray Photoelectron Spectroscopy (XPS) analysis. XPS was performed on a Thermo Fisher Scientific K-alpha$^+$ spectrometer. Samples were analysed using a micro-focused monochromatic Al X-ray source (72 W) using the "400-micron spot" mode, which provides an analysis defining elliptical X-ray spot of *ca.* 400 × 600 microns. Data was recorded at pass energies of 150 eV for survey scans and 50 eV for high resolution scans with step sizes of 1 eV and 0.1 eV respectively, the dwell time was 50 ms and 10 ms in each case. The minimal number of scans per region were acquired to minimise any degradation which is well known with the XPS analysis of battery materials. Samples were mounted in an argon filled glove box in a Thermo scientific vacuum transfer module (VTM) which was then evacuated to *ca.* 10^{-3} mbar for a period of 30 minutes in the glove box ante-chamber prior to transferring to the spectrometer (time taken <1 minute) where the VTM was further pumped to $< 5 \times 10^{-7}$ mbar.

Data analysis was performed in CasaXPS v2.3.27[66] after calibrating the data to the lowest C (1s) component taken to have a value of 284.5 eV for graphitic carbon or 285 eV for organic species. Quantification was made using a Shirley type background and Scofield cross sections, with an electron energy dependence based on the TPP-2M relationship.[67]

Author contributions

DMCO designed the experiments, prepared the manuscript and performed the electrolyte salt synthesis, NMR study, electrochemical studies and cell cycling. JMC assisted with the analysis of the electrochemistry results and recorded SEM and digital microscope images of the aluminium foils. DJM performed the XPS measurements, fitting and assisted with the XPS analysis. DJC acquired and analysed the viscometric data. MWO, SJ and BdB provided the electrodes for sodium-ion cycling. CPG and DSW assisted with the manuscript preparation and analysis. SM provided materials, laboratory infrastructure and resources and oversaw the direction of the project. All authors have read and approved the manuscript.

Conflicts of interest

There are no conflicts to declare.

Data availability

The data supporting this article have been included as part of the Supplementary information (SI). Supplementary information: electrochemistry figures, XPS spectra, SEM images and NMR spectra. See DOI: https://doi.org/10.1039/d6eb00011h.

Acknowledgements

SM acknowledges support from the Royal Society through an Industry Fellowship (IF\R2\23200112). DMCO and SM also acknowledge funding from the Faraday Institution through the Industry SPRINT programme (grant number FIRG074) and Batri Ltd for supply of hard carbon. DMCO, CPG and DSW would like to thank the Faraday Institution FIRG064 and FIRG089 for supporting this work. XPS data collection was performed at the Cardiff hub of the EPSRC National Facility for X-ray photoelectron spectroscopy, the EPSRC National Facility for XPS ("HarwellXPS", EP/Y023587/1, EP/Y023609/1, EP/Y023536/1, EP/Y023552/1 and EP/Y023544/1).

References

1 T. Kim, W. Song, D.-Y. Son, L. K. Ono and Y. Qi, *J. Mater. Chem. A*, 2019, **7**, 2942–2964.
2 M. Armand, P. Axmann, D. Bresser, M. Copley, K. Edström, C. Ekberg, D. Guyomard, B. Lestriez, P. Novák, M. Petranikova, W. Porcher, S. Trabesinger, M. Wohlfahrt-Mehrens and H. Zhang, *J. Power Sources*, 2020, **479**, 228708.
3 M. Dixit, B. Witherspoon, N. Muralidharan, M. M. Mench, C.-B. M. Kweon, Y.-K. Sun and I. Belharouak, *ACS Energy Lett.*, 2024, **9**, 3780–3789.
4 C. P. Grey and D. S. Hall, *Nat. Commun.*, 2020, **11**, 6279.
5 S. Qiao, Q. Zhou, M. Ma, H. K. Liu, S. X. Dou and S. Chong, *ACS Nano*, 2023, **17**, 11220–11252.
6 H. Moon, A. Innocenti, H. Liu, H. Zhang, M. Weil, M. Zarrabeitia and S. Passerini, *ChemSusChem*, 2023, **16**, e202201713.
7 Y. Xiao, J. Xiao, H. Zhao, J. Li, G. Zhang, D. Zhang, X. Guo, H. Gao, Y. Wang, J. Chen, G. Wang and H. Liu, *Small*, 2024, **20**, 2401957.
8 R. Sun and Y. You, *ACS Appl. Mater. Interfaces*, 2023, **15**, 44599–44606.
9 A. Ponrouch, D. Monti, A. Boschin, B. Steen, P. Johansson and M. R. Palacín, *J. Mater. Chem. A*, 2015, **3**, 22–42.
10 A. Ponrouch, E. Marchante, M. Courty, J.-M. Tarascon and M. R. Palacín, *Energy Environ. Sci.*, 2012, **5**, 8572–8583.
11 F. Cheng, M. Cao, Q. Li, C. Fang, J. Han and Y. Huang, *ACS Nano*, 2023, **17**, 18608–18615.
12 P. Barnes, K. Smith, R. Parrish, C. Jones, P. Skinner, E. Storch, Q. White, C. Deng, D. Karsann, M. L. Lau, J. J. Dumais, E. J. Dufek and H. Xiong, *J. Power Sources*, 2020, **447**, 227363.
13 E. Cho, J. Mun, O. B. Chae, O. M. Kwon, H.-T. Kim, J. H. Ryu, Y. G. Kim and S. M. Oh, *Electrochem. Commun.*, 2012, **22**, 1–3.
14 Y. Yamada, C. H. Chiang, K. Sodeyama, J. Wang, Y. Tateyama and A. Yamada, *ChemElectroChem*, 2015, **2**, 1687–1694.
15 K. M. Scheer, M. Tulloch, I. Hamam, J. J. Abraham, M. B. Johnson and M. Metzger, *J. Electrochem. Soc.*, 2025, **172**, 010511.
16 L. O. S. Colbin, C. A. Hall, A. S. Etman, A. Buckel, L. Nyholm and R. Younesi, *Energy Adv.*, 2023, **3**, 143–148.
17 L. G. Chagas, S. Jeong, I. Hasa and S. Passerini, *ACS Appl. Mater. Interfaces*, 2019, **11**, 22278–22289.
18 J. Serra Moreno, G. Maresca, S. Panero, B. Scrosati and G. B. Appetecchi, *Electrochem. Commun.*, 2014, **43**, 1–4.
19 D. Reber, R. Figi, R.-S. Kühnel and C. Battaglia, *Electrochim. Acta*, 2019, **321**, 134644.
20 S. Di Muzio, A. Paolone and S. Brutti, *J. Electrochem. Soc.*, 2021, **168**, 100514.
21 D. Monti, E. Jónsson, A. Boschin, M. R. Palacín, A. Ponrouch and P. Johansson, *Phys. Chem. Chem. Phys.*, 2020, **22**, 22768–22777.
22 J. Welch, R. Mogensen, W. van Ekeren, H. Eriksson, A. J. Naylor and R. Younesi, *J. Electrochem. Soc.*, 2022, **169**, 120523.
23 R. Mogensen, S. Colbin, A. S. Menon, E. Björklund and R. Younesi, *ACS Appl. Energy Mater.*, 2020, **3**, 4974–4982.
24 R. Mogensen, A. Buckel, S. Colbin and R. Younesi, *Chem. Mater.*, 2021, **33**, 1130–1139.
25 R. Mogensen, S. Colbin and R. Younesi, *Batter. Supercaps*, 2021, **4**, 791–814.
26 M. Xia, H. Chen, Z. Zheng, Q. Meng, A. Zhao, X. Chen, X. Ai, Y. Fang and Y. Cao, *Adv. Energy Mater.*, 2025, **15**, 2403306.
27 Z. Cheng, Z. Zhang, M. Wu, M. Jia, X. Du, Z. Gao, S. Tong, T. Wang, X. Yan, X. Zhang and H. Zhou, *Angew. Chem., Int. Ed.*, 2025, **64**, e202503864.

28 X. Liu, J. Zhao, H. Dong, L. Zhang, H. Zhang, Y. Gao, X. Zhou, L. Zhang, L. Li, Y. Liu, S. Chou, W. Lai, C. Zhang and S. Chou, *Adv. Funct. Mater.*, 2024, **34**, 2402310.
29 D. M. C. Ould, S. Menkin, H. E. Smith, V. Riesgo-Gonzalez, E. Jónsson, C. A. O'Keefe, F. Coowar, J. Barker, A. D. Bond, C. P. Grey and D. S. Wright, *Angew. Chem., Int. Ed.*, 2022, **61**, e202202133.
30 B. Roy, P. Cherepanov, C. Nguyen, C. Forsyth, U. Pal, T. C. Mendes, P. Howlett, M. Forsyth, D. MacFarlane and M. Kar, *Adv. Energy Mater.*, 2021, **11**, 2101422.
31 Z. Li, O. Fuhr, M. Fichtner and Z. Zhao-Karger, *Energy Environ. Sci.*, 2019, **12**, 3496–3501.
32 A. Shyamsunder, L. E. Blanc, A. Assoud and L. F. Nazar, *ACS Energy Lett.*, 2019, **4**, 2271–2276.
33 Z. Zhang, Z. Cui, L. Qiao, J. Guan, H. Xu, X. Wang, P. Hu, H. Du, S. Li, X. Zhou, S. Dong, Z. Liu, G. Cui and L. Chen, *Adv. Energy Mater.*, 2017, **7**, 1602055.
34 Z. Zhao-Karger, M. E. G. Bardaji, O. Fuhr and M. Fichtner, *J. Mater. Chem. A*, 2017, **5**, 10815–10820.
35 A. E. Gebala and M. M. Jones, *J. Inorg. Nucl. Chem.*, 1969, **31**, 771–776.
36 L. Terborg, S. Nowak, S. Passerini, M. Winter, U. Karst, P. R. Haddad and P. N. Nesterenko, *Anal. Chim. Acta*, 2012, **714**, 121–126.
37 P. J. Buitrago Botero, A. W. Ells, A. Svirinovsky-Arbeli, M. Juelsholt and L. E. Marbella, *J. Am. Chem. Soc.*, 2025, **147**, 9159–9174.
38 E. W. C. Spotte-Smith, T. B. Petrocelli, H. D. Patel, S. M. Blau and K. A. Persson, *ACS Energy Lett.*, 2023, **8**, 347–355.
39 V. H. Bode and G. Teufer, *Acta Cryst.*, 1956, **9**, 825–826.
40 I. A. Guzei and J. M. Langenhan, *Acta Cryst.*, 2003, **C59**, i95–i96.
41 M. Metzger, B. Strehle, S. Solchenbach and H. A. Gasteiger, *J. Electrochem. Soc.*, 2016, **163**, A1219–A1225.
42 B. L. D. Rinkel, D. S. Hall, I. Temprano and C. P. Grey, *J. Am. Chem. Soc.*, 2020, **142**, 15058–15074.
43 B. L. D. Rinkel, J. P. Vivek, N. Garcia-Araez and C. P. Grey, *Energy Environ. Sci.*, 2022, **15**, 3416–3438.
44 Y. R. Dougassa, J. Jacquemin, L. El Ouatani, C. Tessier and M. Anouti, *J. Phys. Chem. B*, 2014, **118**, 3973–3980.
45 I. Azcarate, W. Yin, C. Méthivier, F. Ribot, C. Laberty-Robert and A. Grimaud, *J. Electrochem. Soc.*, 2020, **167**, 080530.
46 R. He, L. McDonough, L. Seitz, W. Ou, S. D. Marks, R. F. de Menezes, E. Allan-Cole, H. Luo, M. F. Toney, K. G. Sprenger, M. Zhou and R. C. Tenent, *ACS Electrochem.*, 2025, **1**, 494–503.
47 D. W. McOwen, D. M. Seo, O. Borodin, J. Vatamanu, P. D. Boyled and W. A. Henderson, *Energy Environ. Sci.*, 2014, **7**, 416–426.
48 D. M. C. Ould, M. E. Penrod, J. B. McConnell, M. A. Zabara, A. H. Berge, C. A. O'Keefe, A. D. Bond, S. Menkin, C. P. Grey and D. S. Wright, *Chem. Commun.*, 2025, **61**, 129–132.
49 Z. Liu, Z. Lu, S. Guo, Q.-H. Yang and H. Zhou, *ACS Cent. Sci.*, 2023, **9**, 1076–1087.
50 I. Nielsen, C. A. Hall, A.-M. Mattsson, R. Younsei, A. Buckel, G. Ek and W. R. Brant, *J. Mater. Chem. A*, 2024, **12**, 17413–17421.
51 W. R. Brant, R. Mogensen, S. Colbin, D. O. Ojwang, S. Schmid, L. Häggström, T. Ericsson, A. Jaworski, A. J. Pell and R. Younesi, *Chem. Mater.*, 2019, **31**, 7203–7211.
52 E. Peled and S. Menkin, *J. Electrochem. Soc.*, 2017, **164**, A1703–A1719.
53 H. Wang, X. Li, F. Li, X. Liu, S. Yang and J. Ma, *Electrochem. Commun.*, 2021, **122**, 106870.
54 D. O. Ojwang, M. Svensson, C. Njel, R. Mogensen, A. S. Menon, T. Ericsson, L. Häggström, J. Maibach and W. R. Brant, *ACS Appl. Mater. Interfaces*, 2021, **13**, 10054–10063.
55 C. Misiewicz, A. E. Ulander, T. Melin, A. Hall and E. J. Berg, *Adv. Mater. Interfaces*, 2024, 2400854.
56 S. L. Dreyer, F. M. Maddar, A. Kondrakov, J. Janek, I. Hasa and T. Brezesinski, *Batter. Supercaps*, 2024, **7**, e202300595.
57 J. Fondard, E. Irisarri, C. Courrèges, M. R. Palacin, A. Ponrouch and R. Dedryvère, *J. Electrochem. Soc.*, 2020, **167**, 070526.
58 C. Leibing, D. Leistenschneider, C. Neumann, M. Oschatz, A. Turchanin and A. Balducci, *ChemSusChem*, 2023, **16**, e202300161.
59 F. Rahide, J. K. Flowers, J. Hao, H. S. Stein, H. Ehrenberg and S. Dsoke, *J. Electrochem. Soc.*, 2023, **170**, 120534.
60 Y. Pan, Y. Zhang, B. S. Parimalam, C. C. Nguyen, G. Wang and B. L. Lucht, *J. Electroanal. Chem.*, 2017, **799**, 181–186.
61 S. Büchele, V. Mereacre, N. Bohn, P. Stüble, X. Wu, N. Keim, R. Xu, H. Geßwein, W. Sun, G. Vrhovac, M. Pordzik, T. Bergfeldt, S. Indris, W. Bauer, H. Ehrenberg and J. R. Binder, *Batter. Supercaps*, 2025, **8**, e202500015.
62 B. Heidrich, M. Börner, M. Winter and P. Niehoff, *J. Energy Storage*, 2021, **44**, 103208.
63 D. M. C. Ould, S. Menkin, C. A. O'Keefe, F. Coowar, J. Barker, C. P. Grey and D. S. Wright, *Angew. Chem., Int. Ed.*, 2021, **60**, 24882–24887.
64 A. Willow, M. Orzech, S. Kiani, N. Reynolds, M. Houchell, O. Omisore, Z. Tehrani and S. Margadonna, *Batteries*, 2025, **11**, 97.
65 C. Q. X. Lim and Z.-K. Tan, *ACS Appl. Energy Mater.*, 2021, **4**, 6214–6220.
66 N. Fairley, V. Fernandez, M. Richard-Plouet, C. Guillot-Deudon, J. Walton, E. Smith, D. Flahaut, M. Greiner, M. Biesinger, S. Tougaard, D. Morgan and J. Baltrusaitis, *Appl. Surf. Sci. Adv.*, 2021, **5**, 100112.
67 S. Tanuma, C. J. Powell and D. R. Penn, *Surf. Interface Anal.*, 2003, **35**, 268–275.